# Nature of Turbulence inside Small-scale Magnetic Flux Ropes near the Sun: Parker Solar Probe Observations

Zubair I. Shaikh[1,2] , Geeta Vichare[1] , Ankush Bhaskar[3] , Anil N. Raghav[4] , and Sofiane Bourouaine[5,6]
[1] Indian Institute of Geomagnetism, Plot 5, Sector 18, New Panvel, Navi Mumbai-410218, India; zubairshaikh584@gmail.com
[2] Space Sciences Laboratory, University of California at Berkeley, 7 Gauss Way, Berkeley, CA 94720, USA
[3] Space Physics Laboratory, Vikram Sarabhai Space Centre, ISRO, Thiruvananthapuram, 695022, India
[4] University Department of Physics, University of Mumbai, Vidyanagari, Santacruz (E), Mumbai-400098, India
[5] Johns Hopkins Applied Physics Laboratory, 11100 Johns Hopkins Road, Laurel, MD 20723, USA
[6] Department of Aerospace, Physics and Space Sciences, Florida Institute of Technology, 150 University Boulevard, Melbourne, FL 32901, USA
Received 2022 December 5; revised 2023 September 20; accepted 2023 September 20; published 2023 December 5

## Abstract

In this study, we probe the turbulence characteristic within the small-scale magnetic flux ropes (SSMFRs) close to the Sun using Parker Solar Probe (PSP) magnetic field data. The study includes 50 SSMFRs observed by PSP during Encounter 1, 2, and 3 between $35.74\,R_\odot$ and $142.29\,R_\odot$ distance from the Sun. We observed that the average spectral index for all the selected SSMFR events is $-1.49 \pm 0.21$. In line with expectations, we also saw average $|\sigma_m|$ values close to zero throughout the inertial range. We also observed that the size of the eddy at the highest frequency is much smaller than the size of the SSMFRs, indicating anisotropy within it. Thus, our finding supports anisotropic models that feature the Iroshnikov–Kraichnan index. Our findings agree with the turbulence properties of the solar wind near the Sun. We also observe low $\sim0.1$ compressibility, indicating SSMFRs are dominant by Alfvénic fluctuations. In light of this, we believe such an incompressible MHD spectrum results from nonlinear interactions between Alfvénic fluctuations. As a result, our research contributes to understanding the energy cascade process and its transport in solar plasma within the inner heliosphere.

## 1. Introduction

Since its discovery in 1959, the solar wind (SW) has been the subject of extensive research. The in situ measurements, numerical solutions, and simulations suggested that the SW plasma exhibited weak turbulence close to the Sun that gradually developed away from the Sun (Tu & Marsch 1995; Goldstein et al. 1995; Bruno & Carbone 2016; Galtier 2018; Matthaeus 2021). It is thought that either the Sun or the SW's expansion injects energy into the electromagnetic and velocity fluctuations. Turbulence provides a path for the energy transfer from large scale to small scale (spatial/time) through a cascade process until it eventually dissipates (Matthaeus et al. 1999; Sorriso-Valvo et al. 2007; Alexandrova et al. 2008; Andrés et al. 2019; Yang et al. 2019). The power spectral density of magnetic field or velocity generally has three distinct scales, such as injection scales, inertial range, and dissipation scale. These scales are separated by the two spectral breaks. Different scales exhibit different turbulence spectrums, such as $f^{-1}$ injection scales, inertial scale $f^{-5/3}$ to $f^{-3/2}$, and dissipation scale $f^{-2}$ to $f^{-4}$ (Bale et al. 2005; Matthaeus et al. 2007; Kolmogorov 1941; Kraichnan 1965; Bruno & Carbone 2013). The spectral break at low frequency separates the inertial range from (larger) injection scales, whereas, the spectral break at high frequency separates the inertial scale from dissipation scales (e.g., Bruno & Carbone 2013, 2016). Moreover, spectral breakdowns and other turbulence characteristics, such as Alfvénic content, intermittency, and power spectrum

anisotropy, depend on the radial distance from the Sun (see, e.g., Bruno & Trenchi 2014; Bourouaine et al. 2012).

Turbulence plays a significant role in various plasma processes: plasma heating (Yordanova et al. 2021; Perrone et al. 2014; Chandran et al. 2013), particle acceleration (e.g., Petrosian 2012; Brunetti & Lazarian 2007), particle modulation (e.g., Shalchi 2020), structure and dynamics of the Earth's magnetosphere (such as energy and mass influx; e.g., Borovsky & Funsten 2003), anisotropy (Sahraoui et al. 2006; Chen et al. 2010; Horbury et al. 2012), generation of coherent structures (Karimabadi et al. 2013; Wan et al. 2016; Grošelj et al. 2019), and so on (Bruno & Carbone 2016). Generally, Kolmogorov found an analytical expression of the inertial-range spectrum as $-5/3$ for isotropic MHD turbulence (Kolmogorov 1991). Moreover, in turbulent plasma, the cross-scale energy transfer occurs due to nonlinear interactions among fluctuations. It can make the inertial-range spectrum $-3/2$ (Iroshnikov 1963; Kraichnan 1965). Therefore, to accurately represent turbulence, fluctuation amplitudes, nonlinearities, and inhomogeneities must be taken into consideration (e.g., Bruno & Carbone 2013). Furthermore, several numerical simulations suggest that the decay of the fully developed SW turbulence can generate coherent structures (e.g., small-scale magnetic flux-ropes (SSMFRs); Zhao et al. 2019a; Servidio et al. 2009; Zheng & Hu 2018).

A magnetic flux rope (MFR) is a structure in which magnetic field lines tangle up around a central axis with a greater axial magnetic field (Zurbuchen & Richardson 2006). In situ observation of small-scale magnetic flux ropes (SSMFRs) has been claimed within the SW at several heliospheric distances (e.g., Moldwin et al. 2000; Cartwright & Moldwin 2010; Chen et al. 2020b; Chen & Hu 2022). They found the scale size of

the SSMFRs ranges from $\geqslant 10$ minutes to $\leqslant 1$ hr, and is more likely observed in the slow SW rather than fast SW (Cartwright & Moldwin 2008; Feng et al. 2008). Recently, Zhao et al. (2020, 2021) developed a new SSMFR identification routine based on MHD invariant: (i) the normalized reduced magnetic helicity, (ii) the normalized cross helicity, and (iii) the normalized residual energy. Their results for SSMFR properties in the first four Parker Solar Probe (PSP) orbits are consistent with statistical results at 1 au (Yu et al. 2014). The researcher also used the Grad–Shafranov (GS) technique to study SSMFRs (e.g., Hu et al. 2018; Chen et al. 2019) and suggested that the properties of SSMFRs vary with latitudes, radial distances, and under different solar activities or SW conditions. Recently, Chen et al. (2020b) and Chen & Hu (2022) observed SSMFRs close to the Sun from 0.13 to 0.66 au using PSP spacecraft. Moreover, the signature of counterstreaming suprathermal electron, unidirectional beams (Strahl), (sunward) conic distributions, etc., are observed within SSMFRs (Feng et al. 2015; Choi et al. 2021). Gosling et al. (2010) observed torsional Alfvén wave–embedded SSMFRs within the SW. Shi et al. (2021) found the existence of Alfvén waves (proton cyclotron waves) inside (at the outer boundary) SSMFRs at about 0.2 au using PSP measurements. Recently, Teh (2021) studied the thermodynamics of SSMFRs and noted the effective polytropic index closer to 5/3 with torsional Alfvén wave–embedded SSMFRs, as compared to those without. It is believed that SSMFRs are manifestations of solar eruptions similar to magnetic clouds (Feng et al. 2008; Cartwright & Moldwin 2010) or local magnetic reconnection in the SW/current sheet (Moldwin et al. 1995, 2000; Cartwright & Moldwin 2008), the solar corona and the SW (Huang et al. 2020a), etc. Moreover, Xu et al. (2020) noted maximum SSMFRs outside ICMEs near the Earth, thus having different origins (compared to coronal mass ejections (CMEs)). It suggests that the origin of SSMFRs is debatable; they can originate in the SW or corona.

Furthermore, various theories and simulations depict that the interaction of multiple magnetic flux ropes can accelerate charged particles due to magnetic reconnection (e.g., Drake et al. 2006; Khabarova et al. 2015; Le Roux et al. 2016, 2018; Zhao et al. 2019a). In this context, Drake et al. (2006) proposed Fermi acceleration due to magnetic field line contraction, whereas Oka et al. (2010) suggested direct acceleration by antireconnection electric fields associated with the merging of magnetic islands or flux ropes. Furthermore, Zank et al. (2014) developed a transport equation describing the particle acceleration in a "sea" of interacting magnetic islands. They also suggested a power-law-like energy spectrum. Zhao et al. (2018, 2019a) observed a typical energetic particle event using the Ulysses spacecraft, which follows the good agreement of the Zank et al. (2014) transport model prediction. Similar, observations were reported by Khabarova et al. (2015, 2016) and Adhikari et al. (2019) at 1 au. Furthermore, SW also has Alfvénic flux-rope structures, which have the characteristic of slab turbulence. It is suggested that such structures contribute to particle energization due to stochastic heating (e.g., Chandran et al. 2013). Zhao et al. (2018) developed a general theory of stochastic particle acceleration via magnetic reconnection processes, which can explain particle acceleration due to observed SSMFRs near 5 and 84 au (Zhao et al. 2019b). Van Eck et al. (2022) investigated such particle acceleration scenarios in the inner heliosphere using Helios observations.

They suggest that the second-order Fermi acceleration mechanism (dominated by the turbulent motional electric field parallel to the background field) by SSMFRs is more important than first-order Fermi acceleration due to the mean compression of the SSMFRs regions. Thus, SSMFRs play a significant role in particle acceleration. However, it remains an open problem: what is the nature of turbulence within the SSMFR structures close to the Sun? Here, we will explore the nature of turbulence within the SSMFRs using PSP data close to the Sun during the first, second, and third encounters.

## 2. Data and Methodology

Our study includes plasma data from the Solar Wind Electrons, Alphas, and Protons Investigation Solar Probe Cup (Kasper et al. 2016) and magnetic field data (in Radial Tangential Normal coordinates) from Electromagnetic Fields Investigation (Bale et al. 2016) instruments on board the PSP spacecraft.[7] The temporal resolution of the data is about 0.874 s for plasma moments and 0.25 s for the magnetic field vector. Furthermore, we have utilized a catalog[8] that provides a list of SSMFRs during the first (24), second (20), and third (32) PSP encounters between 2018 October and 2019 September at a distance from $\sim$35 to $\sim$142 $R_\odot$. Thus, we analyzed 76 SSMFR events to understand their turbulent characteristics. Note that the list of SSMFRs available on the above website is identified based on the GS reconstruction technique (Chen et al. 2020b, 2021b; Chen & Hu 2022). We do agree that different identification criteria may give different SSMFR databases.

We applied fast Fourier transformation (FFT) on magnetic field data to derive turbulence characteristics within the SSMFRs. The power-law dependency of the magnetic field power spectral density (PSD), i.e., $\mathrm{PSD}(f) \propto f^{-\alpha}$, describes the turbulence characteristic. The scale of the turbulence in the frequency domain (spacecraft frame) is obtained in the range from $\sim$20 mHz to $\sim$2.0 Hz. Note that we have taken a two-point average of the PSD and then fitted it with the power law to find the spectral slope. Furthermore, we compute the normalized magnetic helicity spectrum, $\sigma_m$, as (Matthaeus et al. 1999; Alexandrova et al. 2008)

$$\sigma_m(f) = \frac{2 Im[B_T(f)^* \cdot B_N(f)]}{|B_R(f)|^2 + |B_T(f)|^2 + |B_N(f)|^2}, \qquad (1)$$

where $B_{R,T,N}(f)$ are the Fourier-transformed interplanetary magnetic field (IMF) components. Note that the SSMFRs events have helical magnetic field topology, which means that ideally, the average abs($\sigma_m$) should be $\sim$1 or at least >0.5. But it is important to note that the $\sigma_m$ values at scales smaller than the flux-rope length scale are related to the turbulent fluctuations inside the flux rope, not to the rope structure itself. Only $\sigma_m$ at the very largest scales/smallest frequencies relates to the rope directly. The fact that in SSMFRs the $\sigma_m$ spectra average to approximately zero throughout the inertial range is to be expected (e.g., Smith 2003; Podesta & Borovsky 2010, and references therein). Moreover, another purpose of calculating $\sigma_m$ in our analysis is to identify the role of wave activity within SSMFR to understand the dissipation region. It is a well-known fact that ion cyclotron waves (ICWs)
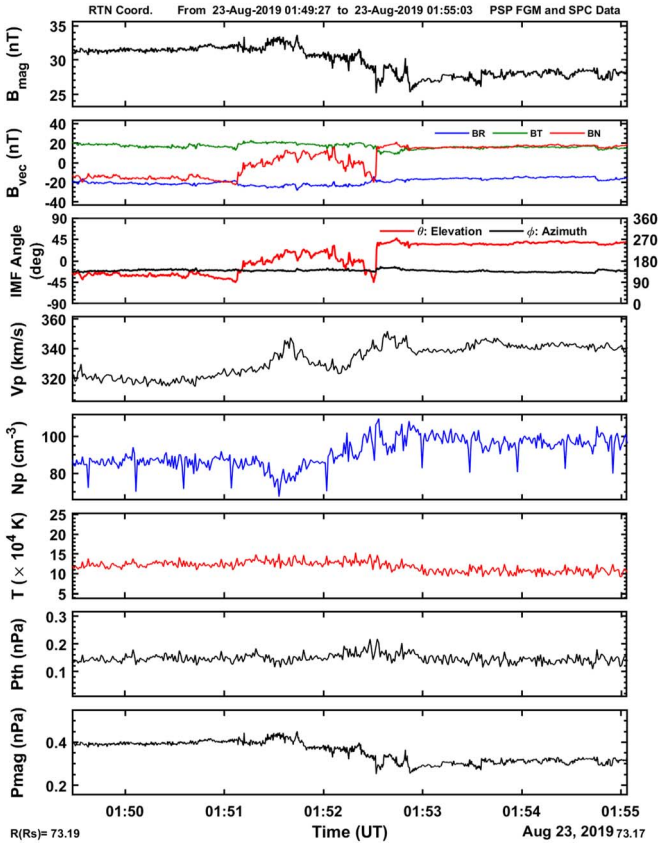
---

**Figure 1.** Temporal profile of plasma parameters and magnetic field during SSMFRs observed by the PSP spacecraft dated 2019 August 23. The top panels (first, second, and third) represent total IMF ($B_{mag}$), IMF components ($B_{vec} = (BR, BT, \text{and } BN)$), and IMF azimuth ($\phi$) and elevation ($\theta$) angles, respectively. The fourth, fifth, and sixth panels show the variation in plasma speed ($Vp$), density ($Np$), and temperature ($T$), respectively. The last two panels show variations of thermal ($Pth$) and magnetic ($Pmag$) pressures.

and kinetic Alfvén waves are circularly polarized waves with frequencies closest to proton cyclotron frequency ($\Omega_p$); therefore, their identification requires the use of normalized magnetic helicity $\sigma_m$ (e.g., Podesta & Gary 2011; He et al. 2011; Bruno & Telloni 2015; Telloni et al. 2015, 2019, 2020; Huang et al. 2020b). During the presence of wave activity, generally $\sigma_m > 0.5$, and for ICWs the $\sigma_m < 0$ (left-handed polarized), whereas for kinetic Alfvén waves (KAWs) $\sigma_m > 0$ (right-handed polarized). Moreover, to find the role of Alfvénic fluctuation within the SSMFRs, we have also calculated the compressibility as $C(f) = \frac{P(B)}{P(BR) + P(BT) + P(BN)}$, where $P(B)$, $P(BR)$, $P(BT)$, and $P(BN)$ is the PSD of the magnetic field and its components. The highly Alfvénic nature is confirmed by the smaller compressibility factor $C$ (see, e.g., Telloni et al. 2021 and references therein). Furthermore, for each SSMFR, we have also estimated (1) the size of the event by multiplying the duration of the event with the average plasma speed and (2) the average Larmor radius ($R_L$; see the definition in Appendix A) of the proton.

### 3. Example Events

Figure 1 demonstrates an example of an SSMFR event observed by the PSP spacecraft on 2019 August 23 from 01:49 to 01:56 UT. The event was detected at about 73.19 $R_\odot$ (about
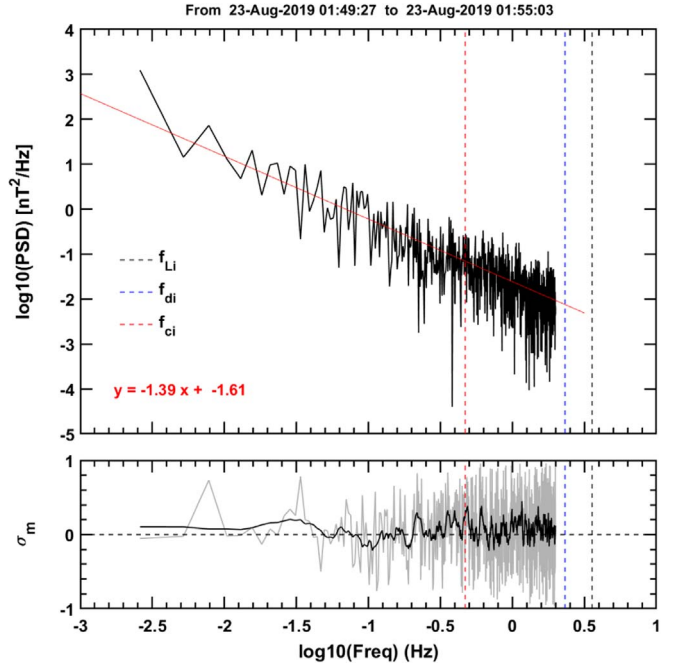


**Figure 2.** The top panel shows FFT-based power spectral density of magnetic field data during the passage of SSMFRs as a function of the spacecraft frequency. The red dashed line shows power-law fitting (95% confidence bound) during the frequency interval from 20 mHz to 2 Hz. The bottom panel represents a plot of magnetic helicity $\sigma_m$ (gray colored plot; as per Equation (1)) as a function of the spacecraft frequency (where the overplotted black plot is a smoothed version of the gray plot). The vertical red dashed line denotes the ion (proton) cyclotron frequency ($f_{ci}$), whereas the vertical blue and black dashed lines denote the frequency corresponding to the ion inertia length ($f_{di}$) and ion Larmor radius ($f_{Li}$), respectively.

0.34 au) distance from the Sun. The first panel shows total IMF, where we observe high magnetic field strength at the leading part, decreasing as the spacecraft passes through the SSMFR. At the same time, the IMF components represent the radial component ($BR$) toward the Sun and do not show significant variation. In contrast, the $BT$ tangential component shows a steady positive value throughout the interval. Whereas the magnitude of $BN$ (normal) at the leading part is lower (negative value) compared to the trailing part (positive value). The transition from negative to positive in $BN$ occurs at 01:52.5 UT. The IMF's azimuth ($\phi$) angle does not vary significantly during the SSMFR transit. The elevation ($\theta$) angle shows the change in orientation from the south to the north direction. The following panels show variations in the plasma speed ($Vp$) and proton density ($Np$). At the leading edge of SSMFR, we observe low values of $Vp$ and $Np$ with steady variation. After 01:51.5, UT both increases and attains maximum value and remains steady again as we move toward the trailing part. Further panels show Temperature ($T$) and thermal pressure ($Pth$) that remain almost steady throughout the transit. The magnetic pressure ($Pmag$) behavior is the same as the IMF total. In summary, we observe a transition in plasma and magnetic field during the interval of 01:51.5 to 01:53, whereas in the remaining time, they are in a steady state. The estimated size of these SSMFRs is $\sim 1.12 \times 10^5$ km, which is estimated by multiplying the event duration (5.6 minutes) with the average $Vp = 332.60$ km s$^{-1}$.

Further, we have applied FFT to the total IMF and get the PSD (see Figure 2). Since the temporal resolution of the magnetic field is 4 Hz, the maximum frequency information we
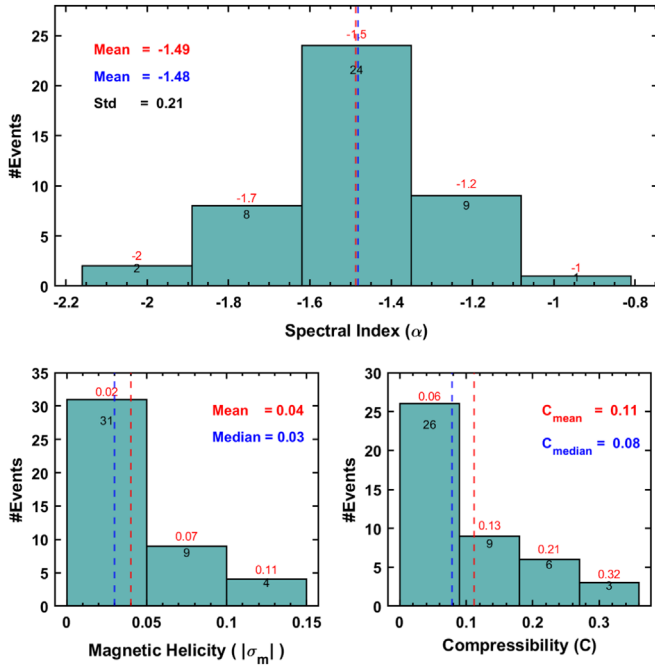
**Figure 3.** Histogram plot of the 44 SSMFR turbulent parameters: spectral index ($\alpha$; top panel), absolute magnetic helicity ($|\sigma_m|$; bottom left panel), and compressibility ($C$; bottom right panel). The "Std" implies standard deviation.



**Figure 4.** Spectral index estimation for Figure 1 (in the main text) but with linear fitting to log10(f) vs. log10(PSD) in the frequency ranges (1) 3–30 mHz, and (2) 50 mHz–1.0 Hz. We highlighted the data points during the fitting interval for better visibility.

can get is up to 2 Hz only. To get the turbulence characteristics, the power-law fitting is performed to the above plot between 20 mHz and 2 Hz frequency range (see the red line). We observe that $f^{-1.39}$ power fit is best fitted to the above curve (with a 95% confidence bound), which suggests that the nature of turbulence associated with the SSMFR is shallower than but close to the Iroshnikov–Kraichnan (IK) spectrum ($\sim f^{-3/2}$; Iroshnikov 1963; Kraichnan 1965), indicating underdeveloped turbulence. Furthermore, we observe that the frequency corresponding to proton cyclotron frequency ($f_{ci}$) cut the PSD spectrum at 0.47 Hz, whereas the other two frequencies corresponding to ion inertia length ($f_{di}$) and ion Larmor radius ($f_{Li}$) are beyond the frequency range of the spectrum (see the definition in Appendix A). We also show the magnitude of normalized magnetic helicity ($|\sigma_m|$) during the above frequency range (see the bottom plot in Figure 2). We observe that the average $|\sigma_m|$ during the 20 mHz to 2 Hz frequency range is 0.07 ($\sim$0) as expected. Furthermore, the average compressibility within this frequency range is 0.09. The low compressibility value ($\sim \leqslant 0.1$) suggests that studies of SSMFRs have high Alfvénic fluctuations (Bruno & Carbone 2016; Telloni et al. 2021). Moreover, the average Larmor radius ($R_L$) of the proton during this event is 116.825 km, which is much smaller than the size of SSMFRs. We performed a similar analysis for the rest of the SSMFRs, where we observed that the power-fit analysis is well fitted with 95% confidence bound only for 44 SSMFRs within the above frequency range. So, further analysis is done only for these SSMFRs as listed in Table 1 (see Appendix D). Moreover, Figure 7 shows an additional six SSMFR events' PSD analyses (see Appendix E).

## 4. Result and Discussion

Generally, SW plasma exhibits turbulent characteristics (Bruno & Carbone 2016). The space plasma behavior, including the production of the SW, the acceleration of high-
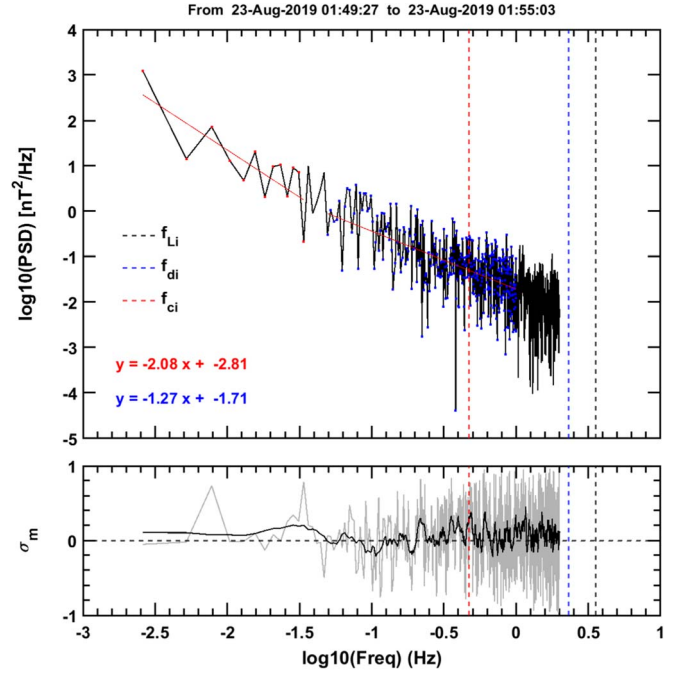
energy particles, plasma heating, and the propagation of cosmic rays, are significantly influenced by turbulence features. Moreover, turbulence shows small-scale fluctuations in velocity and pressure field (for fluids) or in the magnetic field (for plasma) (e.g., Bruno & Carbone 2016; Pope & Pope 2000). It also increases the mass and momentum mixing rate within the region. Since the SW has a mean magnetic field, the low-frequency fluctuations are usually described within the MHD framework that is characterized by a quasi-Kolmogorov energy scaling (Dobrowolny et al. 1980; Matthaeus et al. 1999; Bruno & Carbone 2013; Kolmogorov 1941; Tu & Marsch 1995). In fact, the magnetic energy density seems to follow a spectral decay as $E(k) \propto k^{-5/3}$, although the MHD equation theoretically suggests a slightly different spectral exponent, $E(k) \propto k^{-3/2}$ in the case of Alfvénic turbulence within the SW (Kolmogorov 1941; Kraichnan 1965; Boldyrev 2005, 2006; Perez & Boldyrev 2009).

This extensive statistical analysis presented novel findings on plasma turbulence within the observed SSMFRs near the Sun. The FFT-based turbulence analysis of 44 SSMFRs suggests that the spectral index ranges from −0.87 to −2.06. The top histogram plot in Figure 3 shows the spectral slope distribution for all the studied SSMFRs. The number of events within each bar is shown with a black number, while the average spectral index within each bar is represented with a red number on top of the bar. We observed that the average value of the spectral index, along with the upper and lower bound, is $\alpha = -1.49 \pm 0.21$ while the median value is $-1.48 \pm 0.21$. Thus, our study suggests that the overall spectral index of SSMFR events is close to IK ($\sim f^{-3/2}$) type spectra. It is the same ideal spectral index that is expected for Alfvénic turbulence-rich SW (Iroshnikov 1963; Kraichnan 1965). To verify this, we have calculated compressibility within these SSMFRs. The bottom right plot in Figure 3 represents the distribution of compressibility, which clearly shows that the
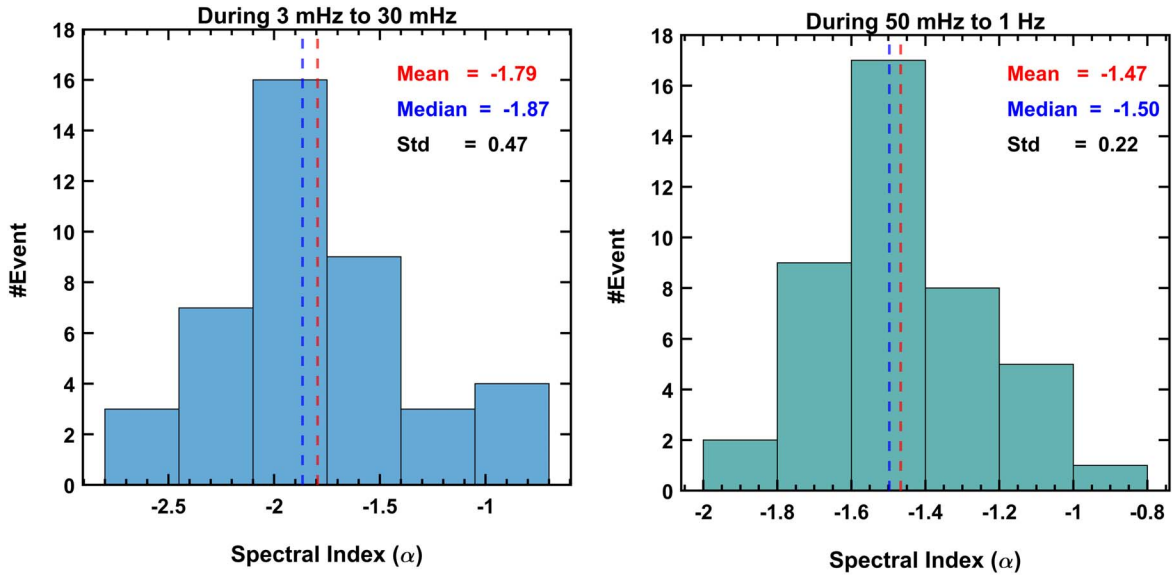
**Figure 5.** The distribution of spectral index (same as Figure 3) for 42 SSMFRs during low-frequency (left) and high-frequency range (right).
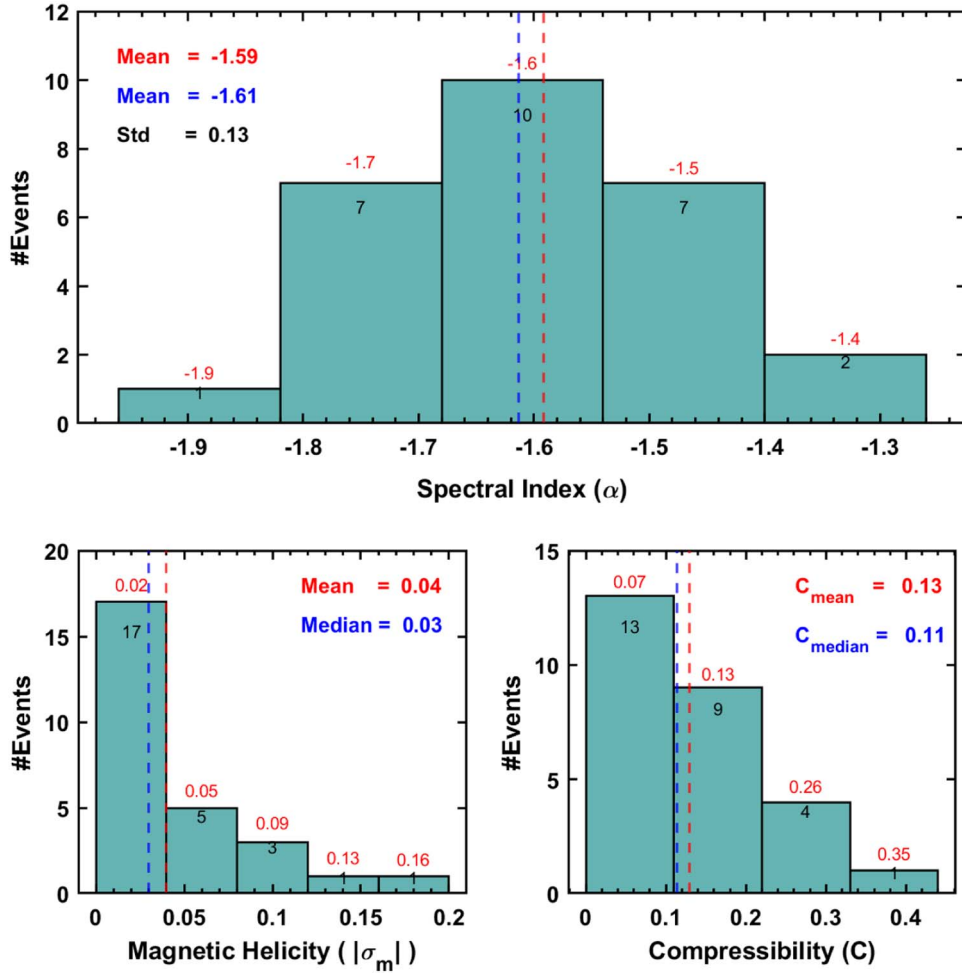


**Figure 6.** Same as Figure 3 but for the case of central 50% data points within the SSMFRs.

average value is 0.11, while the median value is 0.08, respectively. Moreover, maximum data points (26) have an average compressibility of 0.06. The low value of

compressibility suggests that studied SSMFRs are dominant by Alfvénic fluctuations (e.g., Telloni et al. 2021; Bruno & Carbone 2016). Furthermore, the bottom left plot in Figure 3

shows that the average $|\sigma_m| \sim 0.04$ as expected (e.g., Smith 2003; Podesta & Borovsky 2010). Moreover, we did not see any deviation from $\sigma_m \sim 0$ at high frequencies, indicating the absence of the waves (ICW or KAW) associated with the kinetic range. This finding, combined with the absence of any obvious spectral breaks (close to $\Omega_p$), points to the fact that we have not probed kinetic scales within these SSMFR intervals.

Since the fits are weighted toward the high-frequency end of the spectrum, we fit the spectra for two different frequency ranges to see if any low-frequency injection range is present. The two different frequency ranges are (1) low frequency from 3 to 30 mHz and (2) high frequency from 50 mHz to 1 Hz, respectively. We observe that 42 out of 50 SSMFRs show best fitting in both of the frequency ranges. The statistical results are discussed in Appendix B and shown in Figure 5. The average spectral index during the low-frequency interval is $-1.79$ with a standard deviation of 0.47, whereas in the case of the high-frequency range, the average spectral index is $-1.47$ with a standard deviation of 0.22. It clearly indicates that during the low-frequency range, the spectral index is harder compared to the high-frequency range.

In our study, we compared the size of SSMFRs with the smallest eddy associated with the highest observed frequency ($f_m = 2$ Hz) in the inertial range (with the assumption of Taylor's hypothesis: equation $k = \frac{2\pi f_m}{V_p}$, where eddy size ($\eta$) = $1/k$). We noticed that for each event, the $\eta <<$ SSMFRs size. We also found that the width of each SSMFR is wider (3–4 orders of magnitude) compared to the Larmor radius $R_L$; such a wide inertial range is incompatible with the isotropic IK model, indicating the presence of a strong anisotropy (note that the anisotropy in the ropes has only been inferred, not directly calculated). Thus, the observed $\alpha = \sim -3/2$ power spectrum within the SSMFRs supports anisotropic models that feature the IK index (Iroshnikov 1963; Boldyrev 2006). There are recent turbulence models that predicted $-3/2$ in anisotropic turbulence, such as Boldyrev (2006), etc., which rely on what is called the scale-dependent dynamical alignment. The velocity and magnetic turbulence spectra scale as $\sim k^{-3/2}$ for incompressible MHD fluctuations and random interactions between the Alfvén wave packets (Podesta et al. 2007; Bruno & Carbone 2016; Sahraoui et al. 2020).

Previous observations showed that the magnetic spectral index in the inertial range varies depending on the kind of SW: it is shallower for the fast wind ($\alpha = -1.54$) compared to the slow wind ($\alpha = -1.70$) according to in situ measurements made at 1 au by Borovsky (2012). Moreover, the PSP observation (between $\sim 28_\odot$ and $\sim 54_\odot$) suggests that close to the heliospheric current sheet (HCS) the streamer belt wind has lower amplitudes, higher magnetic compressibility, and steeper magnetic field spectrum $-5/3$ (lower Alfvénicity), whereas, away from the HCS spectrum, it is shallower $-3/2$ (e.g., Chen et al. 2021a). Chen et al. (2020a) studied Alfvén wave–dominated SW plasma at 0.17 au ($36 R_\odot$) and noted inertial range spectral indices of $-3/2$. Furthermore, Bourouaine et al. (2020) noted the magnetic power spectrum in the switchback spectral index $\sim -5/3$, whereas $\sim -3/2$ in the nonswitchback. Martinović et al. (2021) noted both $-5/3$ and $-3/2$ spectral index using PSP data inside and near switchbacks. It is proposed that the coherent structures can originate from the turbulent inertial scale (Zheng & Hu 2018; Zank et al. 2020). Note that our study observed the spectral index as

$\alpha = -1.49 \pm 0.21$; we believe SSMFRs are aligned with anisotropic models that feature the IK index. This could signify that the turbulence structure could exhibit strong anisotropy, that is, a strong large-scale magnetic field; therefore, such spectral features are consistent with models of anisotropic turbulence (Boldyrev 2005, 2006). Thus, we believe that our result can also be related to such processes (e.g., Zheng & Hu 2018; Telloni et al. 2021); however, a detailed investigation is needed using either simulation or theory.

Moreover, selecting the SSMFR boundary is crucial because, if boundaries are not properly defined, there are chances of ambient SW contamination within the SSMFRs. Such contamination might affect the turbulent characteristic of SSMFRs. Therefore, to overcome this, we have selected only 50% of the central data points for each SSMFR and performed PSD analysis (see Appendix C). The analysis shows that the average spectral index is $-1.59 \pm 0.13$ (note, in this case, the number of SSMFRs that show the best fit is reduced to 27 only). It suggests that the spectral index is close to the Kolmogorov-spectral index $\sim -5/3$ (see the distribution in Figure 6). It indicates that SSMFRs might have SW contamination at the boundaries; therefore, we need to be cautious while selecting boundaries for SSMFRs.

## 5. Conclusion

Our statistical analysis of SSMFRs suggests the nature of plasma turbulence is closely aligned with anisotropic models that feature the IK ($\sim -3/2$) type index. Moreover, spectra along with low compressibility indicate that the SSMFRs might have greater Alfvénic fluctuations. Thus, we believe the nonlinear interactions between Alfvénic fluctuations make such an incompressible MHD spectrum. It is also possible that the dissipation scale might be present within the SSMFRs at a higher-frequency range or further away from the Sun. Moreover, we also observed that the spectral index is harder in the low-frequency range than in the high-frequency range. Thus, our finding of the turbulence spectrum within the SSMFRs will shed light on energy transport processes from a large to small scale because the heating and acceleration are happening close to the Sun. Moreover, several open questions need a detailed investigation, such as: What is the origin of SSMFRs close to the Sun? Why are dissipation regimes absent in most cases during SSMFR? At what frequency will the spectral break occur? What is the nature of anisotropic turbulence within SSMFRs? etc. Our next step will be to answer these questions to understand better the evolution, dynamics, and role of SSMFRs in the SW.

## Data Availability

The PSP spacecraft data used in this study are publically available at NASA's Coordinated Data Analysis Web (CDA-Web):https://cdaweb.gsfc.nasa.gov/pub/data/psp/, and PSP website https://sppgway.jhuapl.edu/.

## Appendix A
## Definitions of Plasma Parameters

The ion gyroradius (or ion Larmor radius) is defined as $\rho_i = V_{thi}/\Omega_i$, here, $V_{thi} = \sqrt{2k_B T_i/m_i}$ is the ion thermal speed and $\Omega_i = q_i B/m_i$ is the ion gyrofrequency, or $f_{ci} = \Omega_i/2\pi$. The frequency corresponding to the ion Larmor radius is $f_{Li} = V_i/2\pi\rho_i = V_i\Omega_i/V_{thi}$. The ion inertial length is defined as $d_i = c/\omega_{pi} = V_A/\Omega_i$, where $\omega_{pi} = \sqrt{N_i q_i^2/(\epsilon_0 m_i)}$ is the ion plasma frequency and $V_A = B/\sqrt{\mu_0 N_i m_i}$ is Alfvén speed. Furthermore, the frequency corresponding to ion inertia length is given as $f_{di} = V_i/(2\pi d_i)$. Here, $V_i$, $N_i$, $T_i$, and $m_i$ are ion SW speed, number density, temperature, and mass, respectively. $B$, $\mu_0$, and $\epsilon_0$ are magnetic field strength, the permeability of free space, and the permittivity of free space (e.g., Chen et al. 2014).

## Appendix B
## Spectral Index at Low- and High-frequency Ranges

The fitting curve on the PSD of IMF within the SSMFRs is weighted toward the high-frequency end of the spectrum (because there are a lot more points there). Therefore, it is important to see if any low-frequency injection range is present, so we also look into the spectra for two different frequency ranges: (1) low-frequency range from 3 to 30 mHz, and (2) from 50 mHz to 1 Hz, respectively. Figure 4 presents the PSD plot of the same event (Figure 1) discussed in the main text. Here, we can see that during low frequency, the spectral index is −2.08, whereas in the case of the high-frequency range, the index is reduced to −1.27. We noted that 42 out of 50 SSMFRs show best fitting in both frequency ranges. Figure 5 shows the distribution of the spectral index during the low- (left plot) and high-frequency (right plot) range. We noted that the average spectral index during the low-frequency interval is −1.79 with a standard deviation of 0.47, whereas the median spectral index is −1.87. Moreover, in the case of the high-frequency range, the average spectral index is −1.47 with a standard deviation of 0.22, and the median spectral index is −1.50. It demonstrates unequivocally that the spectral index is harder in the low-frequency region than in the high-frequency range.

## Appendix C
## Effect of SSMFR Boundary on the Spectral Index Estimation

Similarly, Figure 6 shows the distribution of spectral index for the selected central 50% data within the SSMFRs. Here, we observe that only 27 SSMFRs show best fitting with 95% confidence bound; thus, the study includes only 27 SSMFRs to derive spectral features. We observe that the mean and median value of the spectral index is $\alpha = -1.59 \pm 0.13$ and $-1.61 \pm 0.13$. It implies that the central 50% of data within the SSMFRs show spectral features close to the Kolmogorov-type spectrum. Moreover, the average and median compressibilities are 0.13 and 0.11, suggesting Alfvénic fluctuations are present within the region. Thus, we found that the original SSMFR boundary and SSMFRs with 50% central data have significantly different spectral index and compressibility. It suggests that those listed in the catalog might have large SW contamination. Thus, we need to take care of the selection of SSMFR boundaries while analyzing turbulence properties.

## Appendix D
## List of Examined SSMFRs

Table 1 provides the list of SSMFR events used in our study observed by PSP spacecraft during encounters 1, 2, and 3. The complete list of SSMFRs is available.[9]

---

[9] http://fluxrope.info/index.html

**Table 1**
List of SSMFR Events and Associated Average Plasma Parameters

| Event Start (Date and Time) (1) | Event End (Date and Time) (2) | $\Delta T$ (minutes) (3) | $B_{mag}$ (nT) (4) | $V_p$ (km s$^{-1}$) (5) | $T_p$ (K) (6) | $N_p$ (cm$^{-3}$) (7) | $P_{mag}$ (nPa) (8) | $P_{th}$ (nPa) (9) | $P_{sw}$ (nPa) (10) | $R_{psp}$ ($R_\odot$) (11) | $\sigma_m$ ... (12) | Spec. Index. $\alpha$ (13) | Comp. $C$ (14) | $R_L$ (km) (15) | SSMFR Size (km) (16) | $f_{ci}$ (Hz) (17) | $f_{Li}$ (Hz) (18) | $f_{di}$ (Hz) (19) | Eddy Size (km) (20) |
|---|---|---|---|---|---|---|---|---|---|---|---|---|---|---|---|---|---|---|---|
| 10/31/2018 0:20 | 10/31/2018 0:36 | 16.33 | 42.49 | 311.35 | 65,307.60 | 164.35 | 0.72 | 0.15 | 26.66 | 56.06 | 0.03 | $-1.62 \pm 0.05$ | 0.08 | 8.07 | 305,120.71 | 0.68 | 6.41 | 2.91 | 24.79 |
| 10/31/2018 0:49 | 10/31/2018 0:55 | 6.07 | 44.08 | 323.58 | 55,226.99 | 136.81 | 0.77 | 0.11 | 23.94 | 55.99 | -0.001 | $-1.52 \pm 0.09$ | 0.19 | 7.15 | 117,782.06 | 0.70 | 7.51 | 2.76 | 25.76 |
| 10/31/2018 3:36 | 10/31/2018 3:45 | 8.87 | 41.57 | 347.08 | 121,965.57 | 194.54 | 0.69 | 0.33 | 39.16 | 55.43 | -0.02 | $-1.56 \pm 0.07$ | 0.08 | 11.27 | 184,645.93 | 0.66 | 5.11 | 3.53 | 27.63 |
| 11/2/2018 12:23 | 11/2/2018 12:29 | 6.07 | 45.93 | 343.92 | 215,730.02 | 202.91 | 0.86 | 0.61 | 40.31 | 44.58 | -0.09 | $-1.49 \pm 0.06$ | 0.04 | 13.57 | 125,186.76 | 0.73 | 4.21 | 3.57 | 27.38 |
| 11/2/2018 12:29 | 11/2/2018 13:21 | 51.80 | 65.27 | 321.07 | 167,000.73 | 195.79 | 1.74 | 0.46 | 33.73 | 44.49 | -0.10 | $-1.53 \pm 0.02$ | 0.06 | 8.39 | 997,886.96 | 1.04 | 6.35 | 3.28 | 25.56 |
| 11/4/2018 19:50 | 11/4/2018 19:57 | 6.07 | 86.04 | 322.76 | 188,361.49 | 277.29 | 2.95 | 0.72 | 48.31 | 37.04 | 0.01 | $-1.40 \pm 0.07$ | 0.07 | 6.77 | 117,483.74 | 1.37 | 7.92 | 3.92 | 25.69 |
| 11/4/2018 20:46 | 11/4/2018 21:34 | 48.07 | 96.21 | 307.06 | 173,550.09 | 306.88 | 3.71 | 0.74 | 48.59 | 36.94 | -0.07 | $-1.1 \pm 0.02$ | 0.04 | 5.81 | 885,567.49 | 1.53 | 8.78 | 3.92 | 24.45 |
| 11/11/2018 22:08 | 11/11/2018 22:19 | 11.67 | 52.22 | 393.26 | 199,938.57 | 216.35 | 1.09 | 0.59 | 55.95 | 54.42 | 0.02 | $-1.38 \pm 0.04$ | 0.11 | 11.49 | 275,281.18 | 0.83 | 5.68 | 4.22 | 31.31 |
| 11/12/2018 2:39 | 11/12/2018 2:47 | 8.40 | 95.21 | 381.61 | 35,779.36 | 113.74 | 3.61 | 0.06 | 27.67 | 55.33 | -0.02 | $-1.39 \pm 0.07$ | 0.01 | 2.67 | 192,332.71 | 1.51 | 23.77 | 2.97 | 30.38 |
| 11/12/2018 2:50 | 11/12/2018 2:58 | 8.87 | 98.03 | 384.06 | 49,839.22 | 108.43 | 3.82 | 0.07 | 26.73 | 55.36 | 0.02 | $-1.69 \pm 0.07$ | 0.02 | 3.06 | 204,319.83 | 1.56 | 20.87 | 2.92 | 30.58 |
| 11/13/2018 9:49 | 11/13/2018 12:09 | 139.53 | 27.71 | 350.65 | 63,740.85 | 227.87 | 0.33 | 0.20 | 46.89 | 61.86 | 0.02 | $-1.72 \pm 0.02$ | 0.28 | 12.22 | 2,935,665.26 | 0.44 | 4.76 | 3.86 | 27.92 |
| 11/13/2018 23:12 | 11/13/2018 23:41 | 28.93 | 27.85 | 323.79 | 64,907.71 | 198.80 | 0.31 | 0.18 | 34.85 | 64.39 | -0.04 | $-1.60 \pm 0.04$ | 0.22 | 12.27 | 562,101.36 | 0.44 | 4.38 | 3.33 | 25.78 |
| 11/14/2018 2:32 | 11/14/2018 2:41 | 8.87 | 31.65 | 319.17 | 67,616.89 | 202.66 | 0.40 | 0.19 | 34.52 | 65.03 | 0.04 | $-1.48 \pm 0.07$ | 0.09 | 11.02 | 169,798.62 | 0.50 | 4.81 | 3.31 | 25.41 |
| 11/14/2018 17:30 | 11/14/2018 17:50 | 19.60 | 34.76 | 390.25 | 194,539.51 | 95.47 | 0.48 | 0.26 | 24.32 | 68.06 | 0.02 | $-1.61 \pm 0.04$ | 0.07 | 17.02 | 458,931.63 | 0.55 | 3.81 | 2.78 | 31.07 |
| 3/13/2019 1:19 | 3/13/2019 5:56 | 276.27 | 12.79 | 289.84 | 48,250.48 | 74.96 | 0.07 | 0.05 | 10.46 | 125.56 | -0.02 | $-1.59 \pm 0.01$ | 0.36 | 23.03 | 4,804,296.96 | 0.20 | 2.09 | 1.83 | 23.08 |
| 3/14/2019 17:24 | 3/14/2019 17:30 | 6.07 | 12.77 | 313.53 | 67,870.56 | 44.15 | 0.07 | 0.04 | 7.25 | 120.26 | -0.11 | $-1.02 \pm 0.08$ | 0.15 | 27.36 | 114,123.08 | 0.20 | 1.90 | 1.52 | 24.96 |
| 3/27/2019 10:35 | 3/27/2019 10:42 | 7.00 | 23.57 | 324.27 | 135,012.99 | 96.57 | 0.22 | 0.18 | 16.97 | 67.62 | 0.02 | $-1.87 \pm 0.06$ | 0.22 | 20.91 | 136,191.94 | 0.38 | 2.57 | 2.32 | 25.82 |
| 4/1/2019 14:15 | 4/1/2019 14:39 | 23.33 | 45.42 | 301.33 | 186,455.69 | 240.53 | 0.83 | 0.63 | 36.47 | 43.41 | 0.09 | $-1.39 \pm 0.04$ | 0.04 | 12.75 | 421,857.19 | 0.72 | 3.92 | 3.41 | 23.99 |
| 4/2/2019 15:47 | 4/2/2019 15:56 | 8.40 | 69.39 | 299.79 | 188,400.27 | 276.04 | 1.97 | 0.73 | 41.32 | 39.58 | -0.10 | $-1.58 \pm 0.05$ | 0.20 | 8.39 | 151,095.38 | 1.10 | 5.93 | 3.63 | 23.87 |
| 4/4/2019 5:55 | 4/4/2019 6:05 | 10.27 | 101.98 | 305.80 | 131,626.74 | 132.26 | 4.14 | 0.24 | 20.66 | 36.07 | 0.05 | $-1.27 \pm 0.06$ | 0.04 | 4.77 | 188,373.22 | 1.62 | 10.64 | 2.56 | 24.35 |
| 4/4/2019 16:11 | 4/4/2019 16:25 | 14.00 | 107.88 | 410.17 | 162,566.71 | 100.04 | 4.63 | 0.23 | 28.21 | 35.74 | 0.004 | $-1.36 \pm 0.04$ | 0.03 | 5.01 | 344,539.54 | 1.715 | 13.58 | 2.99 | 32.66 |
| 4/6/2019 13:08 | 4/6/2019 13:13 | 5.60 | 94.36 | 271.78 | 58,704.36 | 179.99 | 3.54 | 0.15 | 22.18 | 37.68 | 0.000 | $-1.43 \pm 0.07$ | 0.08 | 3.44 | 91,316.88 | 1.50 | 13.10 | 2.66 | 21.64 |
| 4/7/2019 22:29 | 4/7/2019 22:39 | 9.33 | 59.57 | 382.42 | 237,136.71 | 172.46 | 1.43 | 0.58 | 42.18 | 42.06 | 0.02 | $-1.62 \pm 0.05$ | 0.09 | 10.96 | 214,156.50 | 0.95 | 5.79 | 3.66 | 30.45 |
| 4/18/2019 15:07 | 4/18/2019 15:16 | 8.87 | 13.31 | 557.82 | 92,096.43 | 21.05 | 0.07 | 0.03 | 10.17 | 91.32 | 0.02 | $-1.31 \pm 0.07$ | 0.19 | 30.58 | 296,760.64 | 0.21 | 3.03 | 1.87 | 44.41 |
| 8/22/2019 22:35 | 8/22/2019 22:54 | 19.60 | 27.59 | 326.59 | 163,877.02 | 37.86 | 0.30 | 0.09 | 6.78 | 73.79 | 0.03 | $-1.77 \pm 0.04$ | 0.10 | 19.68 | 384,072.28 | 0.439 | 2.75 | 1.47 | 26.00 |
| 8/23/2019 1:49 | 8/23/2019 1:55 | 5.60 | 29.72 | 332.61 | 117,917.73 | 91.25 | 0.35 | 0.15 | 16.95 | 73.18 | 0.07 | $-1.39 \pm 0.06$ | 0.09 | 15.49 | 111,755.34 | 0.47 | 3.56 | 2.32 | 26.48 |
| 8/24/2019 8:25 | 8/24/2019 9:21 | 55.53 | 37.54 | 336.75 | 185,164.73 | 89.07 | 0.57 | 0.23 | 16.89 | 67.00 | 0.04 | $-1.22 \pm 0.03$ | 0.06 | 15.38 | 1,122,039.66 | 0.59 | 3.64 | 2.32 | 26.81 |
| 8/24/2019 9:44 | 8/24/2019 9:50 | 6.07 | 32.65 | 368.73 | 185,096.39 | 93.79 | 0.45 | 0.25 | 21.35 | 66.82 | 0.01 | $-2.06 \pm 0.09$ | 0.33 | 17.68 | 134,215.89 | 0.52 | 3.46 | 2.60 | 29.36 |
| 8/24/2019 15:12 | 8/24/2019 15:26 | 14.00 | 28.55 | 408.12 | 233,472.30 | 69.99 | 0.33 | 0.23 | 19.54 | 65.71 | -0.06 | $-1.36 \pm 0.07$ | 0.07 | 22.69 | 342,823.39 | 0.45 | 2.98 | 2.49 | 32.49 |
| 8/24/2019 16:46 | 8/24/2019 17:22 | 35.93 | 24.88 | 414.19 | 263,054.60 | 55.59 | 0.25 | 0.20 | 15.95 | 65.36 | -0.11 | $-1.62 \pm 0.04$ | 0.07 | 27.65 | 893,011.47 | 0.39 | 2.49 | 2.25 | 32.98 |
| 8/25/2019 3:06 | 8/25/2019 3:25 | 19.60 | 35.98 | 319.11 | 115,096.78 | 111.29 | 0.52 | 0.17 | 18.82 | 63.29 | 0.04 | $-1.57 \pm 0.03$ | 0.08 | 12.65 | 375,275.23 | 0.57 | 4.19 | 2.45 | 25.41 |
| 8/25/2019 12:58 | 8/25/2019 13:10 | 11.67 | 40.74 | 385.76 | 166,325.93 | 51.09 | 0.66 | 0.12 | 12.72 | 61.30 | 0.01 | $-1.33 \pm 0.05$ | 0.04 | 13.43 | 270,029.49 | 0.65 | 4.77 | 2.01 | 30.71 |
| 8/26/2019 2:20 | 8/26/2019 3:15 | 55.07 | 27.72 | 319.03 | 126,361.86 | 133.43 | 0.32 | 0.24 | 22.62 | 58.52 | -0.08 | $-1.54 \pm 0.02$ | 0.12 | 17.19 | 1,054,063.85 | 0.44 | 3.08 | 2.69 | 25.40 |
| 8/26/2019 3:19 | 8/26/2019 3:26 | 7.47 | 34.23 | 316.93 | 142,624.99 | 135.82 | 0.47 | 0.27 | 22.83 | 58.39 | 0.04 | $-1.33 \pm 0.05$ | 0.10 | 14.80 | 141,984.93 | 0.54 | 3.56 | 2.69 | 25.23 |
| 8/26/2019 3:51 | 8/26/2019 5:04 | 72.33 | 34.68 | 317.84 | 133,603.02 | 179.14 | 0.49 | 0.33 | 30.28 | 58.18 | 0.05 | $-1.44 \pm 0.01$ | 0.15 | 14.14 | 1,379,426.24 | 0.55 | 3.73 | 3.10 | 25.31 |
| 8/26/2019 5:24 | 8/26/2019 5:34 | 10.27 | 38.25 | 335.84 | 162,360.51 | 165.54 | 0.58 | 0.37 | 31.23 | 57.97 | 0.04 | $-1.36 \pm 0.05$ | 0.09 | 14.13 | 206,875.33 | 0.61 | 3.95 | 3.15 | 26.74 |
| 8/26/2019 21:31 | 8/26/2019 22:31 | 60.20 | 46.28 | 371.47 | 300,427.93 | 86.37 | 0.85 | 0.36 | 19.96 | 54.63 | -0.06 | $-1.58 \pm 0.02$ | 0.07 | 15.89 | 1,341,742.33 | 0.74 | 3.88 | 2.52 | 29.58 |
| 8/26/2019 22:33 | 8/26/2019 22:46 | 13.07 | 44.29 | 380.67 | 303,784.12 | 87.24 | 0.78 | 0.37 | 21.11 | 54.51 | 0.05 | $-1.14 \pm 0.04$ | 0.05 | 16.69 | 298,445.47 | 0.70 | 3.79 | 2.59 | 30.31 |
| 8/26/2019 22:49 | 8/26/2019 22:57 | 8.40 | 44.54 | 372.14 | 261,013.54 | 88.11 | 0.79 | 0.32 | 20.38 | 54.46 | -0.01 | $-1.28 \pm 0.06$ | 0.07 | 15.39 | 187,558.53 | 0.71 | 4.02 | 2.55 | 29.63 |
| 8/27/2019 19:19 | 8/27/2019 19:29 | 10.27 | 50.97 | 326.54 | 249,724.01 | 93.00 | 1.03 | 0.33 | 16.58 | 50.40 | -0.12 | $-1.59 \pm 0.05$ | 0.08 | 13.15 | 201,145.51 | 0.81 | 4.12 | 2.30 | 26.00 |
| 8/28/2019 9:32 | 8/28/2019 9:55 | 23.33 | 62.57 | 382.92 | 239,088.32 | 79.37 | 1.56 | 0.26 | 19.40 | 47.67 | -0.02 | $-1.26 \pm 0.03$ | 0.05 | 10.48 | 536,093.79 | 1.00 | 6.06 | 2.49 | 30.49 |
| 9/19/2019 3:56 | 9/19/2019 4:10 | 13.07 | 11.76 | 329.09 | 43,971.14 | 47.14 | 0.06 | 0.03 | 8.48 | 106.48 | 0.05 | $-1.40 \pm 0.04$ | 0.23 | 23.93 | 258,005.37 | 0.19 | 2.28 | 1.65 | 26.20 |
| 9/19/2019 16:09 | 9/19/2019 16:21 | 11.67 | 15.87 | 457.05 | 234,890.04 | 32.83 | 0.10 | 0.11 | 11.48 | 108.42 | -0.02 | $-1.99 \pm 0.09$ | 0.16 | 40.95 | 319,935.94 | 0.25 | 1.85 | 1.91 | 36.39 |
| 9/28/2019 14:21 | 9/28/2019 15:00 | 39.20 | 12.12 | 338.57 | 31,660.78 | 25.17 | 0.06 | 0.01 | 4.69 | 138.17 | 0.02 | $-1.68 \pm 0.02$ | 0.15 | 19.69 | 796,324.77 | 0.19 | 2.85 | 1.24 | 26.96 |

The columns show the start of SSMFR, end of SSMFRs, duration of SSMFRs ($\Delta T$), IMF magnitude ($B_{mag}$), plasma proton speed ($V_p$), plasma temperature ($T_p$), plasma density ($N_p$), and pressures, such as magnetic ($P_{mag}$), thermal ($P_{th}$), and dynamics ($P_{sw}$), respectively. Further columns demonstrate the distance of PSP spacecraft ($R_{psp}$), magnetic helicity ($\sigma_m$), spectral index ($\alpha$), compressibility ($C$), proton Larmor radius ($R_L = \frac{m_p V_{th}}{qB}$), and SSMFRs size as described in the main text. The other variables are ion (proton) cyclotron frequency ($f_{ci}$), frequency corresponding to the ion inertia length ($f_{di}$), and ion Larmor radius ($f_{Li}$).

Shaikh et al.

## Appendix E
## Additional Example Events of SSMFRs Turbulence

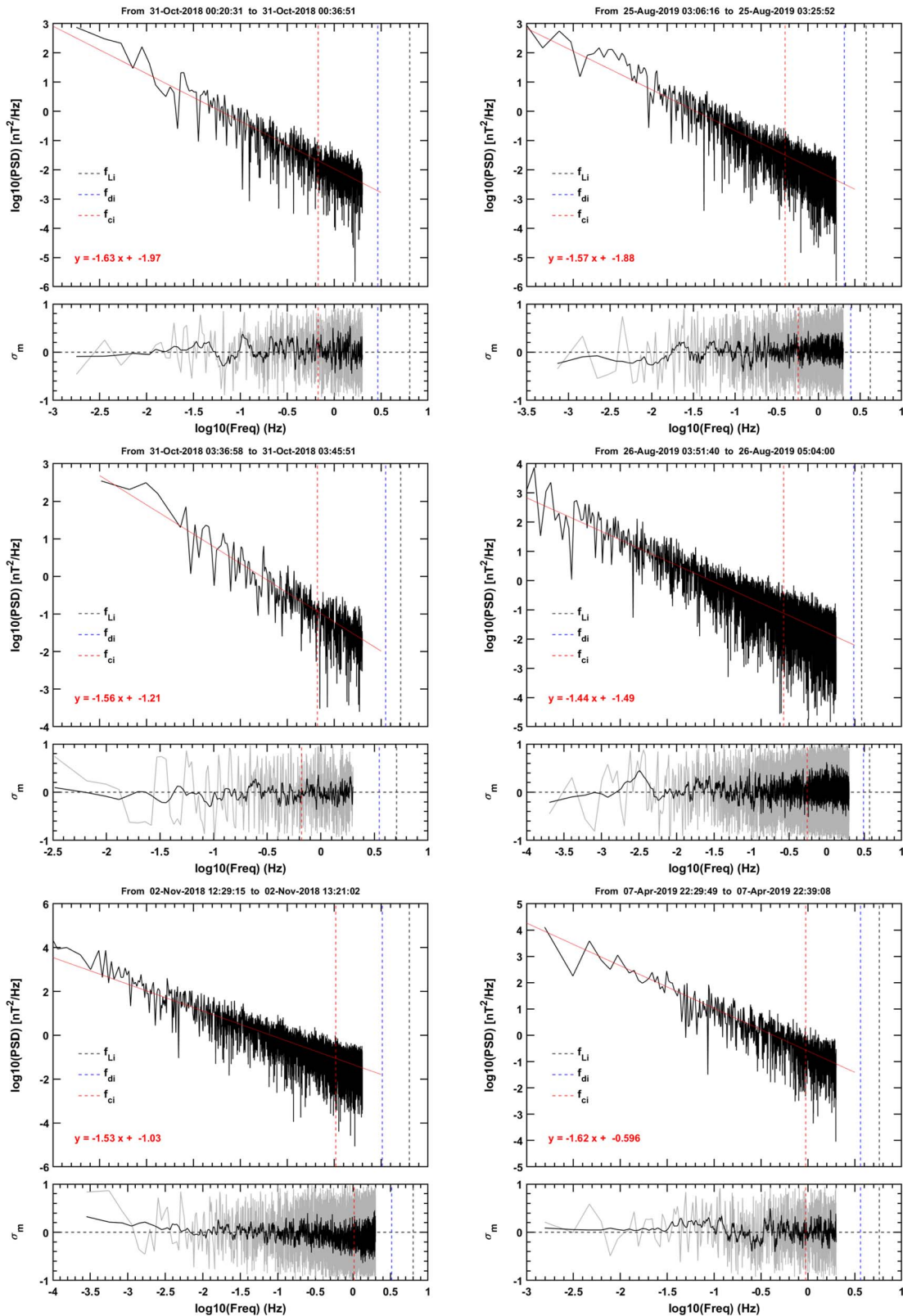Figure 7 shows a list of six additional SSMFRs event's PSD analyses (similar to Figure 2).



**Figure 7.** Same as Figure 2 but for different SSMFRs listed in Table 1.

## ORCID iDs

Zubair I. Shaikh ⓘ https://orcid.org/0000-0002-9206-6327
Geeta Vichare ⓘ https://orcid.org/0000-0003-3607-6923
Ankush Bhaskar ⓘ https://orcid.org/0000-0003-4281-1744
Anil N. Raghav ⓘ https://orcid.org/0000-0002-4704-6706
Sofiane Bourouaine ⓘ https://orcid.org/0000-0002-2358-6628

## References

Adhikari, L., Khabarova, O., Zank, G. P., & Zhao, L. L. 2019, ApJ, 873, 72
Alexandrova, O., Carbone, V., Veltri, P., & Sorriso-Valvo, L. 2008, ApJ, 674, 1153
Andrés, N., Sahraoui, F., Galtier, S., et al. 2019, PhRvL, 123, 245101
Bale, S., Goetz, K., Harvey, P., et al. 2016, SSRv, 204, 49
Bale, S., Kellogg, P., Mozer, F., Horbury, T., & Reme, H. 2005, PhRvL, 94, 215002
Boldyrev, S. 2005, ApJ, 626, L37
Boldyrev, S. 2006, PhRvL, 96, 115002
Borovsky, J. E. 2012, JGRA, 117, A05104
Borovsky, J. E., & Funsten, H. O. 2003, JGRA, 108, 1246
Bourouaine, S., Alexandrova, O., Marsch, E., & Maksimovic, M. 2012, ApJ, 749, 102
Bourouaine, S., Perez, J. C., Klein, K. G., et al. 2020, ApJL, 904, L30
Brunetti, G., & Lazarian, A. 2007, MNRAS, 378, 245
Bruno, R., & Carbone, V. 2013, LRSP, 10, 2
Bruno, R., & Carbone, V. 2016, Turbulence in the Solar Wind, Vol. 928 (Berlin: Springer)
Bruno, R., & Telloni, D. 2015, ApJL, 811, L17
Bruno, R., & Trenchi, L. 2014, ApJL, 787, L24
Cartwright, M., & Moldwin, M. 2008, JGRA, 113, A09105
Cartwright, M., & Moldwin, M. 2010, JGRA, 115, A08102
Chandran, B., Verscharen, D., Quataert, E., et al. 2013, ApJ, 776, 45
Chen, C., Bale, S., Bonnell, J., et al. 2020a, ApJS, 246, 53
Chen, C., Chandran, B., Woodham, L., et al. 2021a, A&A, 650, L3
Chen, C., Horbury, T., Schekochihin, A., et al. 2010, PhRvL, 104, 255002
Chen, C., Leung, L., Boldyrev, S., Maruca, B., & Bale, S. 2014, GeoRL, 41, 8081
Chen, Y., & Hu, Q. 2022, ApJ, 924, 43
Chen, Y., Hu, Q., & le Roux, J. A. 2019, ApJ, 881, 58
Chen, Y., Hu, Q., Zhao, L., et al. 2020b, ApJ, 903, 76
Chen, Y., Hu, Q., Zhao, L., Kasper, J. C., & Huang, J. 2021b, ApJ, 914, 108
Choi, K. E., Lee, D. Y., Wang, H. E., et al. 2021, SoPh, 296, 1
Dobrowolny, M., Mangeney, A., & Veltri, P. 1980, PhRvL, 45, 144
Drake, J., Swisdak, M., Che, H., & Shay, M. 2006, Natur, 443, 553
Feng, H., Wu, D., Lin, C., et al. 2008, JGRA, 113, A12105
Feng, H., Zhao, G., & Wang, J. 2015, JGRA, 120, 10
Galtier, S. 2018, JPhA, 51, 293001
Goldstein, M. L., Roberts, D. A., & Matthaeus, W. 1995, ARA&A, 33, 283
Gosling, J., Teh, W. L., & Eriksson, S. 2010, ApJL, 719, L36
Grošelj, D., Chen, C. H., Mallet, A., et al. 2019, PhRvX, 9, 031037
He, J., Marsch, E., Tu, C., Yao, S., & Tian, H. 2011, ApJ, 731, 85
Horbury, T., Wicks, R., & Chen, C. 2012, SSRvs, 172, 325
Hu, Q., Zheng, J., Chen, Y., le Roux, J., & Zhao, L. 2018, ApJS, 239, 12
Huang, J., Liu, Y., Liu, J., & Shen, Y. 2020a, ApJL, 899, L29
Huang, S., Zhang, J., Sahraoui, F., et al. 2020b, ApJL, 897, L3
Iroshnikov, P. 1963, AZh, 40, 742
Karimabadi, H., Roytershteyn, V., Wan, M., et al. 2013, PhPl, 20, 012303
Kasper, J. C., Abiad, R., Austin, G., et al. 2016, SSRv, 204, 131
Khabarova, O., Zank, G., Li, G., et al. 2015, ApJ, 808, 181
Khabarova, O. V., Zank, G. P., Li, G., et al. 2016, ApJ, 827, 122
Kolmogorov, A. N. 1941, DoSSR, 30, 301
Kolmogorov, A. N. 1991, RSPSA, 434, 9
Kraichnan, R. H. 1965, PhFl, 8, 1385
Le Roux, J., Zank, G., & Khabarova, O. 2018, ApJ, 864, 158
Le Roux, J., Zank, G., Webb, G., & Khabarova, O. 2016, ApJ, 827, 47
Martinović, M. M., Klein, K. G., Huang, J., et al. 2021, ApJ, 912, 28
Matthaeus, W. 2021, PhPl, 28, 032306
Matthaeus, W., Breech, B., Dmitruk, P., et al. 2007, ApJ, 657, L121
Matthaeus, W. H., Zank, G. P., Smith, C. W., & Oughton, S. 1999, PhRvL, 82, 3444
Moldwin, M., Ford, S., Lepping, R., Slavin, J., & Szabo, A. 2000, GeoRL, 27, 57
Moldwin, M., Phillips, J., Gosling, J., et al. 1995, JGR, 100, 19903
Oka, M., Phan, T. D., Krucker, S., Fujimoto, M., & Shinohara, I. 2010, ApJ, 714, 915
Perez, J. C., & Boldyrev, S. 2009, PhRvL, 102, 025003
Perrone, D., Bourouaine, S., Valentini, F., Marsch, E., & Veltri, P. 2014, JGRA, 119, 2400
Petrosian, V. 2012, SSRvs, 173, 535
Podesta, J., & Borovsky, J. 2010, PhPl, 17, 112905
Podesta, J., Roberts, D., & Goldstein, M. 2007, ApJ, 664, 543
Podesta, J. J., & Gary, S. P. 2011, ApJ, 734, 15
Pope, S. B. 2000, Turbulent Flows (Cambridge: Cambridge Univ. Press)
Sahraoui, F., Belmont, G., Rezeau, L., et al. 2006, PhRvL, 96, 075002
Sahraoui, F., Hadid, L., & Huang, S. 2020, RvMPP, 4, 1
Servidio, S., Matthaeus, W., Shay, M., Cassak, P., & Dmitruk, P. 2009, PhRvL, 102, 115003
Shalchi, A. 2020, SSRv, 216, 23
Shi, C., Zhao, J., Huang, J., et al. 2021, ApJL, 908, L19
Smith, C. W. 2003, AdSpR, 32, 1971
Sorriso-Valvo, L., Marino, R., Carbone, V., et al. 2007, PhRvL, 99, 115001
Teh, W. L. 2021, JGRA, 126, e2021JA029944
Telloni, D., Bruno, R., D'Amicis, R., et al. 2020, ApJ, 897, 167
Telloni, D., Bruno, R., & Trenchi, L. 2015, ApJ, 805, 46
Telloni, D., Carbone, F., Bruno, R., et al. 2019, ApJL, 885, L5
Telloni, D., Sorriso-Valvo, L., Woodham, L. D., et al. 2021, ApJL, 912, L21
Tu, C. Y., & Marsch, E. 1995, SSRv, 73, 1
Van Eck, K., le Roux, J., Chen, Y., Zhao, L. L., & Thompson, N. 2022, ApJ, 933, 80
Wan, M., Matthaeus, W., Roytershteyn, V., et al. 2016, PhPl, 23, 042307
Xu, M., Shen, C., Hu, Q., Wang, Y., & Chi, Y. 2020, ApJ, 904, 122
Yang, Y., Wan, M., Matthaeus, W. H., et al. 2019, MNRAS, 482, 4933
Yordanova, E., Vörös, Z., Sorriso-Valvo, L., Dimmock, A. P., & Kilpua, E. 2021, ApJ, 921, 65
Yu, W., Farrugia, C. J., Lugaz, N., et al. 2014, JGRA, 119, 689
Zank, G., Nakanotani, M., Zhao, L. L., Adhikari, L., & Telloni, D. 2020, ApJ, 900, 115
Zank, G. l., Le Roux, J., Webb, G., Dosch, A., & Khabarova, O. 2014, ApJ, 797, 28
Zhao, L. L., Zank, G., Adhikari, L., et al. 2020, ApJS, 246, 26
Zhao, L. L., Zank, G., Chen, Y., et al. 2019a, ApJ, 872, 4
Zhao, L. L., Zank, G., Hu, Q., et al. 2019b, ApJ, 886, 144
Zhao, L. L., Zank, G., Hu, Q., et al. 2021, A & A, 650, A12
Zhao, L. L., Zank, G. P., Khabarova, O., et al. 2018, ApJL, 864, L34
Zheng, J., & Hu, Q. 2018, ApJL, 852, L23
Zurbuchen, T. H., & Richardson, I. G. 2006, in Coronal Mass Ejections, ed. H. Kunow et al. (New York: Springer), 31